

Propagation of optically tunable coherent radiation in a medium of asymmetric molecules

PIOTR GŁADYSZ^{*}, KAROLINA SŁOWIK^{**}

Institute of Physics, Faculty of Physics, Astronomy and Informatics, Nicolaus Copernicus University in Toruń, Grudziadzka 5, 87-100 Torun, Poland

^{*}*glad@doktorant.umk.pl*

^{**}*karolina@fizyka.umk.pl*

Abstract: Coherent, optically dressed media composed of two-level atomic systems without inversion symmetry are considered as all-optically tunable sources of coherent radiation in the microwave to near-infrared domain. Here, a theoretical model and a numerical toolbox are developed to account for buildup and propagation dynamics of such low-frequency impulses in gaseous or bulk media. We discuss the physical mechanisms involved and make a performance study in conditions representative for vapors of heteronuclear diatomic molecules to identify realistic experimental scenarios.

© 2020 Optical Society of America

1. Introduction

Analysis of propagation of electric field in various types of media is a well-known problem in quantum optics, in particular in the context of coherent phenomena [1]. Typically, an ensemble of atoms is dressed with a coherent electromagnetic beam modifying the atomic optical properties probed by a weak pulse or beam of light. Appealing examples include stimulated Raman adiabatic passage [2, 3], magneto-optical rotation [4–6] electromagnetically induced transparency [7–9], light slowdown [10, 11] and storage [12–14].

Despite the long record, there is still room in the field for fundamental and uncharted research ideas even for the simplest possible models. Among such is a one-dimensional medium consisting of two-level systems with broken inversion symmetry, coupled to electromagnetic field.

A two-level system driven by a resonant electromagnetic field is a canonical example considered in quantum optics. Such a system undergoes Rabi oscillations of populations of the two levels as the system subsequently exchanges energy with the driving field. This induces oscillations of a transition dipole moment at the transition frequency. If the inversion symmetry of the two-level system is broken, it additionally generates radiation at the frequency corresponding to the Rabi frequency, i.e. much below the transition frequency between the eigenstates. This can be explained by noting that the permanent electric dipole moment characterizing the system can in general be different in the excited and in the ground state. Thus, the population exchange between the eigenstates corresponds to oscillations of the permanent dipole moment occurring at the Rabi frequency.

Such behaviour was shown firstly in Ref. [15] where coupling of a single asymmetric system with classical light was considered. The discussion was extended to the cases of single-mode and bichromatic light respectively in Ref. [16] and [17]. Nonlinear effects were considered in Ref. [18], where polarizabilities of asymmetric systems were derived. In Refs. [19–21], two-level systems with broken inversion symmetry were suggested for lasing or for generation of squeezed light.

Until now, the analysis neglected field propagation effects. This approach limited possible physical realizations to small amounts of relatively large quantum systems and excluded commonly available molecular clouds or solids. In this paper, we extend that research to scenarios in which a resonant driving beam illuminates an ensemble of two-level systems with broken inversion

symmetry, e.g. representing molecules in a gaseous phase or a bulk anisotropic medium. As a result, a coherent beam of low-frequency radiation is generated throughout the length of the sample and propagates parallel to the drive.

We investigate the performance of the proposed setup as an all-optically-controlled source of coherent radiation. Its frequency could be optically tuned within the microwave - mid infrared domain by modulation of the amplitude of the drive. In an opposite strategy, modulation of the driving field's detuning from resonance with the atomic transition would provide a knob to suppress the outgoing signal at a fixed frequency. To investigate these effects, we develop a method based on the semiclassical Bloch-Maxwell equations derived under a generalized form of the rotating wave approximation. The usual slowly-varying envelope approximation is not applied since it does not hold for low-frequency pulses. The theory is applied to a realistic model of a gaseous medium of molecules, which support a permanent dipole moment.

section Method

1.1. Medium

We consider a quasi-one-dimensional sample containing a medium of uniformly distributed identical two-level systems with broken inversion symmetry. The simplest examples include heteronuclear molecules like carbon oxide (CO), potassium bromide (KBr) or sodium potassium (NaK) [22, 23]. The medium is described with a density matrix $\rho(z, t)$ dependent on position z and time t , which we will describe in the basis of excited (e) and ground (g) states $\{|e\rangle, |g\rangle\}$. The free Hamiltonian of the system can be written as $H_{\text{medium}} = \hbar\omega_0 |e\rangle\langle e|$, where the \hbar stands for the reduced Planck constant, ω_0 is the transition frequency and we have set the energy of the lower state to zero.

The broken inversion symmetry implies that the dipole-moment operator of the system $\hat{\mathbf{d}} = \sum_{ij} \mathbf{d}_{ij} |i\rangle\langle j|$ with $i, j \in \{e, g\}$, has nonzero diagonal elements $|\mathbf{d}_{ii}| \neq 0$ (for a proof please see Appendix A). The diagonal elements correspond to *permanent* dipole moments, in contrast to the usually considered off-diagonal elements describing *transition* dipole moments \mathbf{d}_{ij} with $i \neq j$. The crucial assumption for this work is that the permanent dipole moments of the two eigenstates are not equal $\mathbf{d}_{ee} \neq \mathbf{d}_{gg}$. Please note that the permanent moments enable a parallel alignment of a significant fraction of the two-level systems forming the medium with a DC electric field, and therefore their coherent response to illumination. Naturally, the transition dipole moment $\mathbf{d}_{eg} = \mathbf{d}_{ge}^*$ should be nonzero to enable efficient coupling with the driving electric field, which we describe in the following subsection.

1.2. Electromagnetic field

The electromagnetic field is treated classically. It consists of two components corresponding to the driving and signal fields. Thus, the electric part of the field can be written as

$$\mathbf{E}(z, t) = \mathbf{E}_{\text{drive}}(z, t) + \mathbf{E}_{\text{signal}}(z, t). \quad (1)$$

The drive

$$\mathbf{E}_{\text{drive}}(z, t) = \mathcal{E}(z, t)\mathbf{e} \cos(kz - \omega t), \quad (2)$$

is a strong coherent laser beam of carrier frequency ω close to resonance with the two-level system's transition frequency ω_0 . This usually belongs to the optical or near-infrared regime. Here, \mathbf{e} indicates the polarization of the driving field which we assume constant. The beam propagates along the z direction and on resonance the wavenumber $k = \frac{\omega}{c}$ with c standing for the vacuum speed of light. Tuned close to the resonance with the two-level systems, the driving field induces coherent Rabi oscillations of their population between the ground and excited states. Either due to back-action from the medium or due to external tuning, the envelope \mathcal{E} can be

modulated at time scales comparable to the inverse Rabi frequency. This observation will be important in later parts of this work.

Due to coherent oscillations of population between the eigenstates characterized with unequal permanent dipole moments, a coherent signal field $\mathbf{E}_{\text{signal}}(z, t)$ may be generated in the medium. Its source is the permanent dipole oscillating at the Rabi frequency Ω_R . This is typically in the microwave to mid-infrared regime. Formally, we can distinguish the signal field envelope and a harmonic term

$$\mathbf{E}_{\text{signal}} = \mathcal{E}_s(z, t)\mathbf{e}_s e^{i\Omega_R(\frac{z}{c}-t)} + c.c., \quad (3)$$

where \mathbf{e}_s represents the polarization vector of the signal field, constant and parallel to the permanent dipole moments of the medium. In realistic scenarios, the timescales of modulations of the signal-field envelope may be comparable to the inverse Rabi frequency $|\frac{\partial}{\partial t}\mathcal{E}_s| \lesssim \mathcal{E}_s\Omega_R$, which means that the slowly varying envelope approximation may not be valid for this part of the field and will not be applied. We make a reasonable assumption that initially the signal field is absent throughout the entire sample $|\mathbf{E}_{\text{signal}}(z, t=0)| = 0$ for all $z \in [0, L]$, where L is the sample length. In the following section we derive the equations describing the buildup and propagation of the signal field.

1.3. Medium coupled to the field

The goal of this subsection is to find the coupled Bloch-Maxwell equations that govern the evolution of the density matrix of the medium as well as the propagation of the signal field. In many cases, the propagation effects for the drive can be neglected. Here, we will nevertheless allow temporal tuning of the drive amplitude at reasonable timescales $|\frac{\partial}{\partial t}\mathcal{E}| \ll \mathcal{E}\omega$.

Our starting point is the one-dimensional form of the propagation equation for the total field given by Eq. (1)

$$-\frac{\partial^2}{\partial z^2}\mathbf{E}(z, t) + \frac{1}{c^2}\frac{\partial^2}{\partial t^2}\mathbf{E}(z, t) = -\mu_0\frac{\partial^2}{\partial t^2}\mathbf{P}(z, t), \quad (4)$$

where μ_0 is the vacuum permeability and $\mathbf{P}(z, t)$ is the polarization of the medium. For this equation to be valid, the medium must be nonmagnetic, linear and isotropic, without free charges and currents. We make these assumptions here as they describe a rather wide class of molecular vapours and solids.

The polarization at the right-hand-side of Eq. (4) can be expressed as

$$\mathbf{P}(z, t) = N \text{Tr}(\rho(z, t)\mathbf{d}) = N \sum_{i,j \in \{e,g\}} \rho_{ij}(z, t)\mathbf{d}_{ji}, \quad (5)$$

where N is the concentration of two-level systems in the medium, $\text{Tr}(\cdot)$ stands for the trace operation and $\rho_{ij}(z, t)$ are elements of the density matrix of the medium $\rho(z, t)$. Please note that contrary to the usually considered symmetric case, all density matrix elements contribute to the polarization, including the diagonal ones which give rise to the signal buildup.

In order to find the explicit form of the source term in Eq. (4) we model the evolution of the density matrix with the master equation

$$i\hbar\frac{\partial}{\partial t}\rho(z, t) = [H(z, t), \rho(z, t)] + \mathcal{L}[\rho(z, t)], \quad (6)$$

where H is the full Hamiltonian

$$H(z, t) = H_{\text{medium}} - \mathbf{d} \cdot \mathbf{E}(z, t), \quad (7)$$

H_{medium} was introduced at the beginning of subsection 1.1, and the electric dipole approximation has been assumed for the interaction term. The relaxation term is given by [24, 25]

$$\mathcal{L}[\rho(z, t)] = 2i\hbar \sum_{p=\text{se,dec}} \gamma_p \left(L_p \rho L_p^\dagger - \frac{1}{2}\rho L_p^\dagger L_p - \frac{1}{2}L_p^\dagger L_p \rho \right), \quad (8)$$

where in our system the index $p = \text{"se"}$ corresponds to spontaneous emission with $L_{\text{se}} = |g\rangle\langle e|$, while $p = \text{"dec"}$ describes collisional decoherence $L_{\text{dec}} = |e\rangle\langle e| - |g\rangle\langle g|$. To simplify the notation, we have omitted the arguments of the density matrix on the right-hand side.

From now on we assume that all matrix elements of the dipole moment operator \mathbf{d}_{ij} are oriented in the same direction, parallel to the polarization direction of the fields. Hence, we can omit the vector notation. Please note, however, that the analysis could be equivalently performed for perpendicular orientations of permanent and transition dipoles $\mathbf{d}_{ii} \perp \mathbf{d}_{ij}$, $j \neq i$.

We now insert Eqs. (7) and (1) into the master equation (6) to obtain a set of Bloch equations for the evolution of the elements of the density matrix. To separate slowly-varying and fast-oscillating components of the coherence ρ_{eg} , we adjust the ansatz introduced in Ref. [15]

$$\rho_{eg}(z,t) = \sigma_{eg}(z,t) e^{i(kz-\omega t)} e^{-i\kappa(z,t) \sin(kz-\omega t)}, \quad (9)$$

where the dimensionless parameter $\kappa(z,t) = \frac{\mathcal{E}(z,t)(d_{ee}-d_{gg})}{\hbar\omega}$ is a measure of asymmetry. As we will see from the Bloch equations, the time-scale for variations of the envelope function σ_{eg} is of the order of Ω_R^{-1} .

The last exponent in Eq. (9) can be expressed using the identity $e^{-i\kappa \sin x} = \sum_{n=-\infty}^{+\infty} J_n(\kappa) e^{-inx}$. Making use of this form and inserting Eqs. (7-9) into the master equation (6), with the field in the form given by Eq. (1), we arrive a set of Bloch equations whose general form and detailed derivation are given in Appendix B. The rotating wave approximation leads to the following form of Bloch equations:

$$\frac{\partial}{\partial t} \rho_{ee} = 2 \text{Im}(\Omega_R^* \sigma_{eg}) + 2 \frac{E_{\text{signal}}}{\hbar} J_1(\kappa) \text{Im}(d_{eg}^* \sigma_{eg}) - 2\gamma_{\text{se}} \rho_{ee}, \quad (10a)$$

$$\begin{aligned} \frac{\partial}{\partial t} \sigma_{eg} = i & \left[-\delta + \frac{\partial}{\partial t} \kappa + \frac{E_{\text{signal}}}{\hbar} (d_{ee} - d_{gg}) \right] \sigma_{eg} \\ & + i \left[\Omega_R + \frac{E_{\text{signal}}}{\hbar} J_1(\kappa) d_{eg} \right] (1 - 2\rho_{ee}) - (\gamma_{\text{se}} + \gamma_{\text{dec}}) \sigma_{eg}, \end{aligned} \quad (10b)$$

where we have introduced the detuning $\delta = \omega_0 - \omega \ll \omega_0$ and the Rabi frequency $\Omega_R = \frac{d_{eg}\omega}{d_{ee}-d_{gg}} J_1(\kappa)$. Please note that if the diagonal and off-diagonal terms of the dipole moment are comparable, the order of magnitude for κ corresponds to the ratio of Rabi frequency to the transition frequency in the system. This means that κ is typically small and the Bessel function can be approximated by a linear term $J_1(\kappa) \approx \frac{1}{2}\kappa$. In this regime, the Rabi frequency retrieves the familiar form $\Omega_R \approx \frac{\mathcal{E}(z,t)d_{eg}}{2\hbar}$. It is now clear that the elements ρ_{ee} , σ_{eg} of the density matrix vary at timescales set by Ω_R^{-1} and inverse decoherence rates γ_p^{-1} . From Eq. (10b) it follows that the signal field gives rise to a time- and space-dependent energy shift of the levels, proportional to the difference between the permanent dipole moments of the eigenstates. Additionally, the time dependence of the envelope of the driving field is included in the term $\frac{\partial}{\partial t} \kappa$. This part is negligible for slow changes of the drive's envelope and vanishes for a constant amplitude.

Once we found the evolution of the density matrix elements, we can specify the form of the medium polarization induced by the driving field. Making use of the density matrix normalization $\rho_{gg} + \rho_{ee} = 1$, combining Eqs.(9) and (5) we find

$$\begin{aligned} P(z,t) = N & \left[d_{gg} + \rho_{ee}(d_{ee} - d_{gg}) \right. \\ & \left. + \sigma_{eg} d_{ge} \sum_{n=-\infty}^{\infty} J_n(\kappa) e^{-i(n-1)(kz-\omega t)} + \text{c.c.} \right]. \end{aligned} \quad (11)$$

We can insert this form into the right-hand side of Eq. (4). In order to extract the equation for the signal rather than total field, we insert Eq. (1) to the left-hand-side of Eq. (4). Next,

we separate contributions on both sides of the wave equation oscillating at different harmonic frequencies. This step is based on an assumption that the components of the field oscillating at the Rabi frequency, contributing to the signal, have their source in polarization components oscillating at the Rabi frequency, while their coupling to the polarization components at optical frequencies is negligible [18]. Details of this step are given in Appendix B. As a result, we obtain the propagation equation of the signal field:

$$\begin{aligned}
& -\frac{\partial^2}{\partial z^2} E_{\text{signal}} + \frac{1}{c^2} \frac{\partial^2}{\partial t^2} E_{\text{signal}} = -\mu_0 N (d_{ee} - d_{gg}) \frac{\partial^2}{\partial t^2} \rho_{ee} \\
& - 2\mu_0 N \operatorname{Re} \left\{ d_{ge} \left[J_1(\kappa) \frac{\partial^2}{\partial t^2} \sigma_{eg} + 2J_1'(\kappa) \frac{\partial}{\partial t} \kappa \frac{\partial}{\partial t} \sigma_{eg} \right. \right. \\
& \quad \left. \left. + \left(J_1''(\kappa) \left(\frac{\partial}{\partial t} \kappa \right)^2 + J_1'(\kappa) \frac{\partial^2}{\partial t^2} \kappa \right) \sigma_{eg} \right] \right\}. \tag{12}
\end{aligned}$$

Here, $J_1'(\kappa)$ and $J_1''(\kappa)$ are respectively the first and the second derivative of the Bessel function over the argument κ . These terms represent the influence of temporal modulations of the drive envelope. For a continuous-wave drive all time derivatives of κ disappear and the equation is significantly simplified. In general, $J_1'(\kappa) = \frac{1}{2}[J_0(\kappa) - J_2(\kappa)]$ and $J_1''(\kappa) = \frac{1}{4}[J_3(\kappa) - 3J_1(\kappa)]$. Since typically κ is small, the part proportional to $J_0(\kappa)$ is the dominant contribution. Then, the correction arising from the time-dependence of the drive envelope can be rewritten as $J_0(\kappa) \frac{\partial}{\partial t} \kappa \frac{\partial}{\partial t} \sigma_{eg}$.

From Eq. (12) it follows that both the diagonal and the off-diagonal parts of the density matrix contribute to the generation of low-frequency radiation. Assuming comparable values of permanent and transition dipole moments we see that the oscillation of population has a major impact on signal build-up, in particular in the case of slowly varying drive envelope, i.e. negligible $\frac{\partial}{\partial t} \kappa$. This observation is one of the key points of this work: The physical origin of the generated signal is the permanent dipole moment associated with the eigenstates of the system and oscillating at the Rabi frequency. This is the carrier frequency of the output signal. The Rabi frequency is determined by the drive amplitude \mathcal{E} , which provides a knob for spectral tuning of the signal.

Please note that in many other works the field propagation equation in the Bloch-Maxwell set is a first-order differential equation [8, 14, 26]. That simplified form is obtained under the slowly varying envelope approximation in which the signal envelope is assumed to vary both in time and space much more slowly than its inverse carrier frequency and wave vector, respectively. Here, this approximation may not be justified since the carrier frequency Ω_R is of the same order as the inverse timescales of the system's dynamics and therefore we keep the more complicated second-order propagation equation.

2. Results & Discussion

We apply the theory to a model sample of a gaseous molecular medium characterized with the concentration $N = 6.7 \times 10^{12}$ molecules/cm³. We focus on an electronic transition at $\omega_0 = 660$ THz, with dipole moments set to 1 atomic unit $d_{ee} = d_{eg} = 8.5 \times 10^{-30}$ Cm. The spontaneous emission rate $\gamma_{\text{se}} = 3.4$ MHz is calculated according to the Weisskopf-Wigner theorem [26] and collisional decoherence lifetime $\gamma_{\text{dec}}^{-1} = 15$ μ s has been chosen in accordance with experiments on diluted atomic vapors [27]. The sample of length $L = 53$ cm is illuminated with a driving beam with the envelope

$$\mathcal{E}(t, z) = A \frac{1}{\pi} \left(\arctan(-\alpha(z - z_0 - ct)) + \frac{\pi}{2} \right), \tag{13}$$

where the arctan function was chosen to model a smooth ramp up of the beam. The parameter $\alpha = 0.019/\text{cm}$ is a scaling factor controlling the slope and $z_0 = -5.3$ m. The amplitude $A = 1550$ V/cm corresponds to continuous-wave laser powers of 32 W at a beam area of 1 mm². The resulting shape is shown as the blue curve in Fig. 1a. The carrier frequency of the drive will be chosen around the medium resonance.

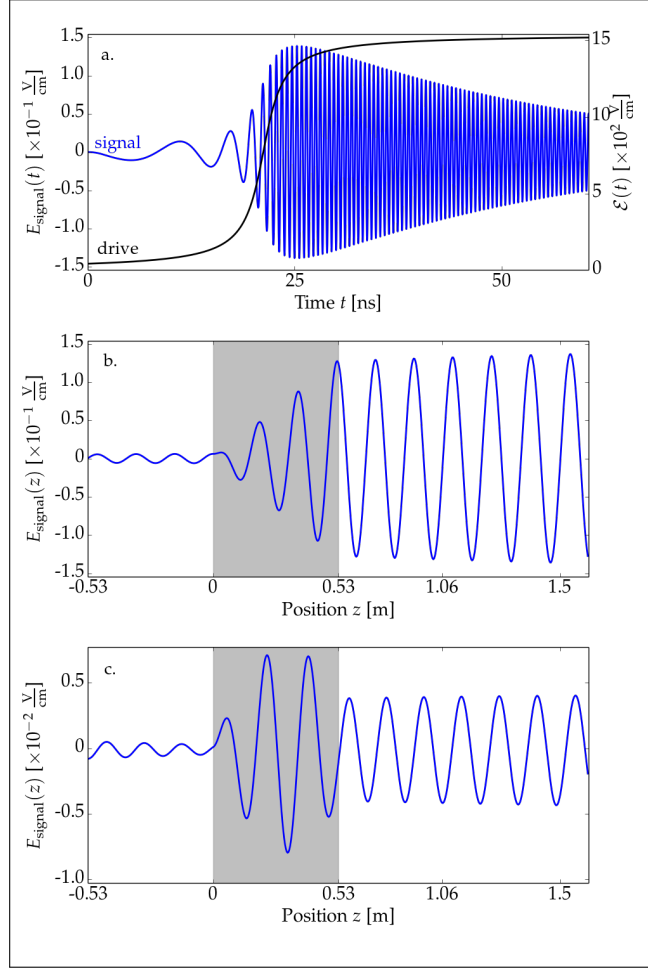


Fig. 1. a. The envelope of the driving field \mathcal{E} (black) and generated signal E_{signal} (blue) as functions of time for $\gamma_{\text{se}} = 3.4$ MHz, $\gamma_{\text{dec}} = 65$ kHz and $\delta = 0$. b. The signal E_{signal} in spatial domain at $t = 30$ ns. The grey rectangle represents the sample with the active medium (between 0 and 0.53 m). c. Spatial behaviour of the generated radiation for the same γ_{se} and γ_{dec} coefficients but in the presence of detuning $\delta = 460$ MHz.

We simulate the Bloch-Maxwell's equations (10,12) with a self-developed Python code, which we make available upon request.

The time-dependence of the generated low-frequency signal at the position fixed at the end of the sample $z = L$ is shown with the blue line in Fig. 1a. As the drive enters the medium, the signal builds up: Please note the signal frequency $\Omega_R(z = L, t)$ varied in time proportionally to the drive envelope $\mathcal{E}(z = L, t)$ and reaching the stable value of 1.97 GHz after about 30 ns. The amplitude of the signal is significantly weaker than the drive, but well beyond the detection threshold in the microwave domain [28,29]. Naturally, the weak amplitude of the signal is a result

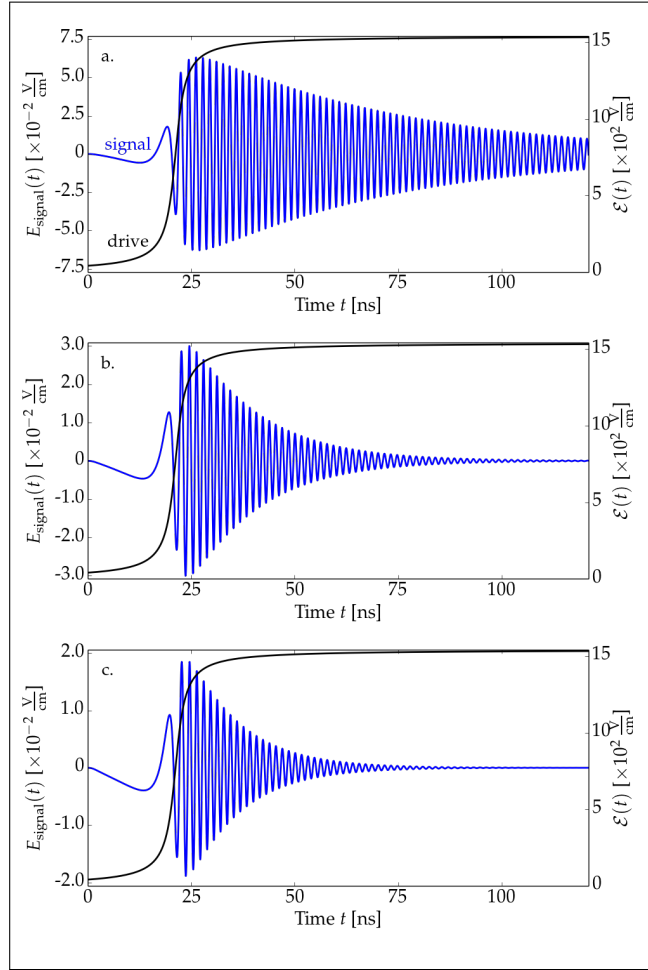


Fig. 2. Shapes of the signal field (blue) for enhanced values of relaxation parameters. The envelope of the driving field is shown in black. a. Only decoherence present $\gamma_{\text{dec}} = 6.6$ MHz, $\gamma_{\text{se}} = 0$. b. Only spontaneous emission involved $\gamma_{\text{se}} = 6.6$ MHz, $\gamma_{\text{dec}} = 0$. c. Full picture $\gamma_{\text{se}} = 6.6$ MHz, $\gamma_{\text{dec}} = 6.6$ MHz.

of the small medium density we have chosen and could be improved in denser samples. Please note that for very large densities at which the mean spatial separation between the molecules would be below the transition wavelength, dipole-dipole interactions of molecules may become relevant which are not included in our model. They could be taken into account e.g. through local-field corrections [30].

Fig. 1b shows the generated signal at a fixed time $E(z, t = 30 \text{ ns})$. The grey area corresponds to $z \in [0, L]$ and represents the active medium, where the amplitude of the signal grows steadily. We find the dominant component of the signal to propagate towards the positive- z direction, in accordance with the propagation direction of the drive. This indicates the coherent character of the generated signal. Outside the sample the signal amplitude retains its value.

Fig. 1c shows the same dependence as Fig. 1b, but for a drive detuned by $\delta = 460$ MHz. Naturally, the generated signal field amplitude is decreased in this case and its frequency shifted, as we will discuss below. Additionally, the detuning induces a beating of the signal field inside the sample, now modulated with a sinusoidal envelope of spatial period corresponding to the

detuning. In consequence, the amplitude of the output signal outside the sample is suppressed depending on the phase of the envelope of the signal at the end of the sample.

Due to decoherence, the signal decays at time scales determined mostly by γ_{se}^{-1} , while γ_{dec} is a relatively less important correction (see Fig. 2). The reason is that the decoherence γ_{dec} does not directly affect the population (i.e. it does not appear in Eq. 10a), which is the main source of the low-frequency signal. The impact of decoherence is through a modification of the coherence term σ_{eg} . The decay of the signal is a direct consequence of decay of population oscillations. This means that the signal can only be generated pulse-wise and in realistic conditions at presence of any relaxation channels, low-frequency signal generation in a continuous manner is not possible.

A close analysis of Eq. (10b) reveals that an effective detuning $\delta_{\text{eff}}(z, t) = \delta - \frac{\partial}{\partial t} \kappa - \frac{E_{\text{signal}}}{\hbar} (d_{ee} - d_{gg})$ can be induced by additional effects: a time-modulation of the drive and a back-action from the generated signal field. While the former is weak for modulation time scales considered in our examples, we analyse the impact of the signal back-action in samples with increased concentration N in Fig. 3. The calculations were performed for a weaker drive ($A = 514$ V/cm), longer time period and the same decoherence parameters for better illustration. In the case of small concentrations the back-action is not observed at investigated time scales (Fig. 3a). For larger medium concentrations, we find a clear indication of the back action from the signal only if we do not include the spontaneous emission (grey curves in Figs. 3b,c): the modulations of the signal amplitude origin from effective time- and space-dependent frequency fluctuation of the atomic transition induced by the signal. However, this effect is blurred at presence of spontaneous emission (blue curves in Figs. 3b,c). The back-action of the signal appears also in Eqs. (10) next to the Rabi frequency Ω_R , modifying it to the effective value $\Omega_{\text{eff}} = \Omega_R + \frac{E_{\text{signal}}}{\hbar} J_1(\kappa) d_{eg}$. Yet, this impact is considerably smaller due to the proportionality of the correction to the Bessel function $J_1(\kappa) \ll 1$.

In order to quantify the impact of the drive detuning on the signal frequency, we evaluate Fourier transforms of the stationary parts of the generated signals (the integration of the signal field $E_{\text{signal}}(z = L, t)$ was performed over times between 72 ns and 121 ns). Their normalized values are shown in Fig. 4. We compare the results obtained numerically for different values of detuning up to $\delta = 657$ MHz, with the theoretical prediction of the oscillation frequency of medium populations [31]¹

$$\Omega = 2\sqrt{\Omega_R^2 + \delta^2/4}. \quad (14)$$

The latter formula is valid for the case of vanishing relaxation rates, while in the studied case $\gamma_{se,dec}$ are around two orders of magnitude smaller than δ . Therefore, the main consequence of relaxation is a spectral broadening of the signal rather than a frequency shift. In the expression above we did not take into consideration the effective parameters Ω_{eff} , δ_{eff} since their influence at the relevant timescale is negligible with respect to the impact of spontaneous emission. The theoretical results are in a very good agreement with the numerical ones, with offsets at the third significant digit, i.e. exactly at the level at which we expect corrections from the relaxations.

The derived Bloch-Maxwell equations allow us to study the generation of low-frequency radiation under more complex illumination schemes than a smooth step function. In Fig. 5 we present the temporal shape of signals generated under illumination with Gaussian impulses defined as:

$$\mathcal{E}(z, t) = Ae^{-\alpha(z-z_0-ct)^2}, \quad (15)$$

where $\alpha = a^2 \times 2.3 \times 10^{-6}/\text{cm}^2$, hence the full temporal width at half-maximum $\text{FWHM}(a) = a \times 12$ ns. The signals have Gaussian envelopes. The frequency chirp result from the drive modulation. The shift of the maximum of the signal with respect to the peak of the drive is due to relaxations and disappears at absence of spontaneous emission and decoherence. Fig. 5c presents fast Fourier

¹The factor of 2 appears because Ω_R corresponds to the frequency of oscillations of probability amplitudes, while the population probabilities are modulated at a doubled pace.

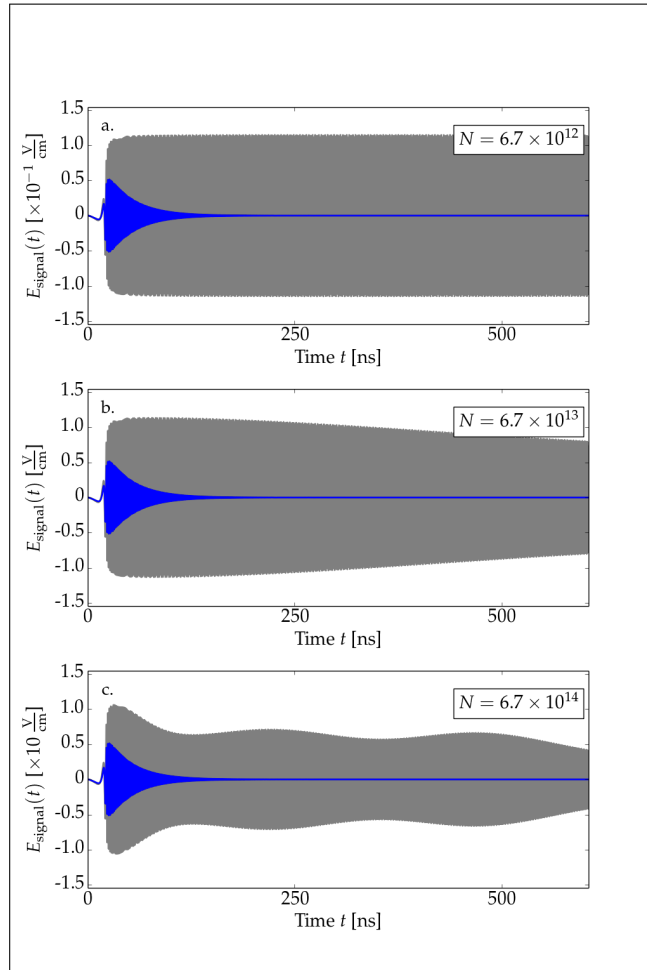


Fig. 3. Generated signal for different concentrations N in the medium with (blue) and without (grey) relaxations. The driving field's amplitude was set to $A = 515$ V/cm. a. Concentration $N = 6.7 \times 10^{12}$ molecules/cm³. b. $N = 6.7 \times 10^{13}$ molecules/cm³. c. $N = 6.7 \times 10^{14}$ molecules/cm³.

transforms (FFTs) of both signals. The main frequencies are $\Omega = 1.93$ GHz and 1.88 GHz for wider and narrower impulses respectively. We observe that for increasing temporal FWHMs of the drive, the main frequency of the signal corresponds to the value of 1.97 GHz which is the continuous wave limit.

Please note that consideration of a pulsed drive brings into perspective a considerable increase of the driving field power, and in consequence the frequency of the signal. In particular, signals in the THz domain could be achieved for the drive peak powers from 3.5 MW, assuming the other system parameters as selected above.

At the end of this section we point out that in order to generate a coherent signal, a co-orientation of the dipole moments of the molecules forming the medium is required. Then, the coupling of each molecule with the drive is equally strong which results in their coherent response. To include a distribution of orientation directions of the molecules, one would need to replace the density N on the right-hand side of Eq. (12) with a distribution function $N(\theta, \phi)$, and integrate over the orientations (θ, ϕ) . In practice, this would suppress the coherence of the generated signal

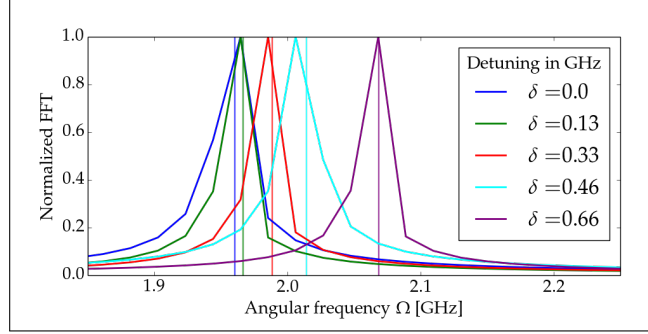


Fig. 4. Fast Fourier transforms (FFT) of the generated signals reveal frequencies of the signals for the resonant case (blue line) and for several values of detuning (other lines), all for $\Omega_R = 1.97$ GHz. The uncertainty for each point is 0.02 GHz. The vertical lines indicate frequencies calculated according to Eq. (14).

due to a distribution of coupling strengths between the differently oriented molecules and the drive. However, co-orientation of molecules sustaining permanent dipole moments could be achieved e.g. with an externally applied static electric field.

3. Conclusions

In conclusion, we have shown how coherent radiation at the Rabi frequency is generated and propagates through a one-dimensional medium consisting of two-level systems with broken inversion symmetry. The underlying mechanism is associated with the Rabi oscillations of population between the eigenstates induced as the resonant drive illuminates the medium, and of the corresponding permanent dipole moments.

To quantify the effect, we derived Bloch-Maxwell equations governing dynamics of the system. The equations were solved numerically for sets of parameters representing standard molecular media. The results confirm that the generation of low-frequency radiation is mostly caused by the oscillations of population in the medium while other contributions can be considered as corrections. The output signal amplitude and frequency can be tuned with drive intensity modulation, allowing for an all-optical control of the signal properties. In our examples the signal frequency belongs to the microwave regime, while the amplitude is small but detectable. A pulsed illumination scheme allows one to increase both intensity and frequency of the signal, potentially leading to tunable sources of coherent THz radiation.

A. Relation between broken inversion symmetry and dipole moment

A diagonal element of the dipole moment operator with $i = e, g$ is given by:

$$\mathbf{d}_{ii} = \langle i | \hat{\mathbf{d}} | i \rangle = \int d\mathbf{r} \sum_{\alpha} q_{\alpha} \mathbf{r}_{\alpha} \langle i | \mathbf{r} \rangle \langle \mathbf{r} | i \rangle, \quad (16)$$

where $\mathbf{r} = \{\mathbf{r}_{\alpha}\}_{\alpha=1, \dots, N}$ represents a set of positions \mathbf{r}_{α} of all N charges q_{α} contributing to the dipole moment of the system. For simplicity we perform this proof assuming a single charge q at position \mathbf{r}_1 . A proof for multiple charges is a straightforward generalization.

To evaluate this quantity we express \mathbf{r}_1 in spherical coordinates defined as follows (Fig. 6):

$$\begin{aligned} x &= r \cos \phi \cos \theta, \\ y &= r \sin \phi \cos \theta, \\ z &= r \sin \theta. \end{aligned} \quad (17)$$

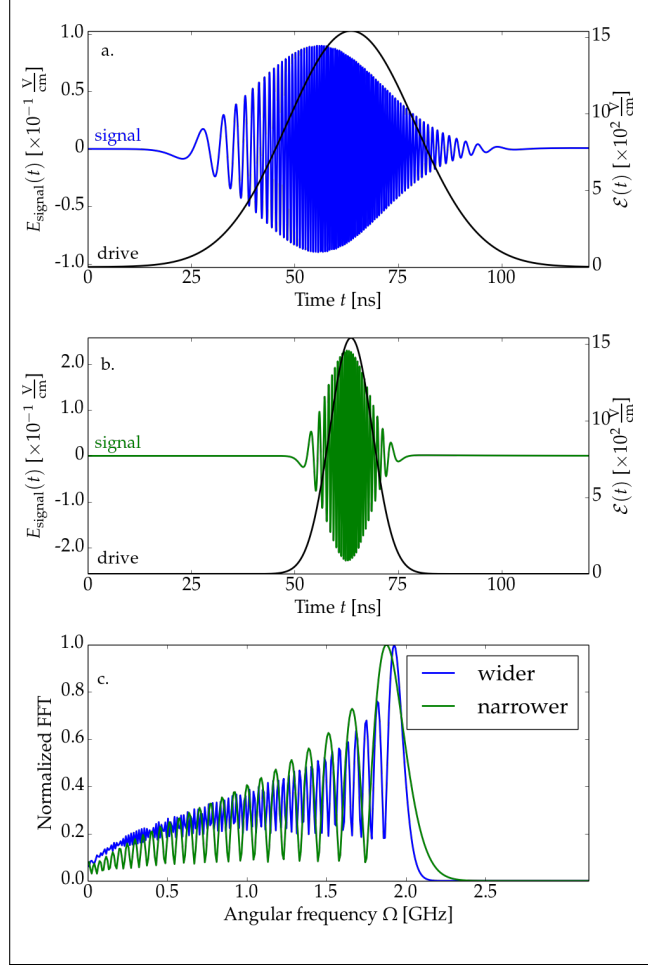


Fig. 5. Results of the simulation for the impulse driving field with amplitude $A = 515 \text{ V/cm}$. Blue and green lines represent generated signal while black ones are envelopes of the drive in form of Gaussians with FWHM respectively a. 36 ns and b. 12 ns. c. Fast Fourier transform performed on signal impulses.

to obtain

$$\begin{aligned}
 \mathbf{d}_{ii} &= q \int_0^\infty dr_1 \int_{-\pi}^\pi d\phi_1 \int_{-\pi/2}^{\pi/2} d\theta_1 r_1^2 \cos \theta_1 \mathbf{r}_1 |\langle \mathbf{r}_1 | i \rangle|^2 \\
 &= q \int_0^\infty dr_1 \int_{-\pi}^\pi d\phi_1 \int_0^{\pi/2} d\theta_1 r_1^2 \cos \theta_1 \mathbf{r}_1 |\langle \mathbf{r}_1 | i \rangle|^2 \\
 &+ q \int_0^\infty dr_1 \int_{-\pi}^\pi d\phi_1 \int_{-\pi/2}^0 d\theta_1 r_1^2 \cos \theta_1 \mathbf{r}_1 |\langle \mathbf{r}_1 | i \rangle|^2
 \end{aligned} \tag{18}$$

By substituting angles $\phi \rightarrow -\phi$, $\theta \rightarrow -\theta$ in the second term and making use of the relation

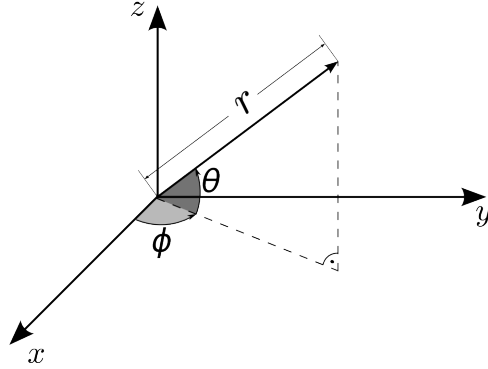


Fig. 6. Spherical coordinates system used in calculations according to (17). Unusual choice of directed angles θ and ϕ (notice the arrows in the picture) was intentional to set limits of integration symmetric in the equations.

$\cos(-\theta) = \cos(\theta)$ we end up with:

$$\mathbf{d}_{ii} = q \int_0^\infty dr_1 \int_{-\pi}^\pi d\phi_1 \int_0^{\pi/2} d\theta_1 r_1^2 \cos \theta_1 \mathbf{r}_1 \times \left(|\langle \mathbf{r}_1 | i \rangle|^2 - | \langle -\mathbf{r}_1 | i \rangle|^2 \right), \quad (19)$$

where $-\mathbf{r}_1 = (r_1, -\phi_1, -\theta_1)$. If the wavefunction $\langle \mathbf{r}_1 | i \rangle$ is characterized with inversion symmetry, $|\langle \mathbf{r}_1 | i \rangle| = |\langle -\mathbf{r}_1 | i \rangle|$ holds and the bracket at the end disappears. This implies that the diagonal elements d_{ee} and d_{gg} are equal to zero. This means that broken inversion symmetry is required to create a permanent dipole moment.

For the off-diagonal elements we simply have:

$$\mathbf{d}_{ij} = \langle i | \hat{\mathbf{d}} | j \rangle = \int d\mathbf{r} \mathbf{r} \langle i | \mathbf{r} \rangle \langle \mathbf{r} | q \hat{\mathbf{r}} | \mathbf{r}_1 \rangle \langle \mathbf{r}_1 | j \rangle = \mathbf{d}_{ji}^*, \quad (20)$$

regardless of the wavefunction's symmetry. Due to the odd character of the position operator, if both wavefunctions share the same symmetry the integral is equal to zero and the transition is electric-dipole forbidden.

B. Bloch-Maxwell's equations

Here, we provide a detailed derivation of the Bloch-Maxwell equations. First of all, let us insert the form of the field given by Eq. (1) into the master equation (6). The set of equations for the density matrix elements has a form:

$$i\hbar \frac{\partial}{\partial t} \rho_{ee} = (\mathcal{E} \cos(kz - \omega t) + E_{\text{signal}}) (d_{ge} \rho_{eg} - d_{eg} \rho_{ge}) - 2i\hbar \gamma_{se} \rho_{ee}, \quad (21a)$$

$$i\hbar \frac{\partial}{\partial t} \rho_{eg} = \hbar \omega_0 \rho_{eg} - (\mathcal{E} \cos(kz - \omega t) + E_{\text{signal}}) \times ((d_{ee} - d_{gg}) \rho_{eg} - d_{eg} (2\rho_{ee} - 1)) - i\hbar (\gamma_{se} + \gamma_{dec}) \rho_{eg}. \quad (21b)$$

Dynamics of the other elements can be found based on the density matrix properties: $\rho_{ee} + \rho_{gg} = 1$ and $\sigma_{ge} = \sigma_{eg}^*$. Next, we make use of the ansatz (9) and expand the κ -dependent term into a series of Bessel functions $e^{-i\kappa \sin x} = \sum_{n=-\infty}^{+\infty} J_n(\kappa) e^{-inx}$:

$$i\hbar \frac{\partial}{\partial t} \rho_{ee} = \left[\frac{1}{2} \mathcal{E} \left(e^{2i(kz-\omega t)} + 1 \right) + E_{\text{signal}} e^{i(kz-\omega t)} \right] \times \sum_{n=-\infty}^{\infty} J_n(\kappa) e^{-in(kz-\omega t)} d_{eg}^* \sigma_{eg} + \text{c.c.} - 2i\hbar \gamma_{se} \rho_{ee}, \quad (22a)$$

$$i\hbar \frac{\partial}{\partial t} \sigma_{eg} = \hbar \left[\delta - \frac{\partial}{\partial t} \kappa - E_{\text{signal}} (d_{ee} - d_{gg}) \right] \sigma_{eg} + \left[\frac{1}{2} \mathcal{E} \left(e^{2i(kz-\omega t)} + 1 \right) + E_{\text{signal}} e^{-i(kz-\omega t)} \right] d_{eg} \times (2\rho_{ee} - 1) \sum_{n=-\infty}^{+\infty} J_n(\kappa) e^{in(kz-\omega t)} - i(\gamma_{es} + \gamma_{dec}) \sigma_{eg}. \quad (22b)$$

If $\Omega_R \ll \omega$, the oscillatory terms on the right-hand side of the above equations make negligible contributions. We neglect them under the rotating wave approximation, in which out of the infinite sums the only surviving terms correspond to $n = 0, 2$ if they are multiplied by the drive envelope \mathcal{E} , or correspond to $n = 1$ if they are multiplied by the signal field. We arrive at the equations from the article (10).

In order to derive formula (12), we insert Eq. (1) into the right-hand side of Eq. (4). Performing all the derivatives we end up with:

$$-\frac{\partial^2}{\partial z^2} E + \frac{1}{c^2} \frac{\partial^2}{\partial t^2} E = -\frac{\partial^2}{\partial z^2} E_{\text{signal}} + \frac{1}{c^2} \frac{\partial^2}{\partial t^2} E_{\text{signal}} + \frac{1}{2} \left(-\frac{\partial^2}{\partial z^2} + \frac{1}{c^2} \frac{\partial^2}{\partial t^2} - 2ik \frac{\partial}{\partial z} + 2i \frac{\omega}{c^2} \frac{\partial}{\partial t} + k^2 - \frac{\omega^2}{c^2} \right) \mathcal{E} \times \left(e^{i(kz-\omega t)} - e^{-i(kz-\omega t)} \right). \quad (23)$$

Clearly, the slowly varying terms of the expression correspond to the signal, while and terms related to the drive envelope are multiplied by rapidly oscillating factors.

Let us now investigate the right-hand-side of the wave equation with the second time derivative of polarization. The fastest method is to apply the derivatives to the form of polarization given by Eq. (11). We introduce the symbol:

$$R = \sum_{n=-\infty}^{\infty} J_n(\kappa) e^{-i(n-1)(kz-\omega t)}. \quad (24)$$

The second time derivative of the polarization reads:

$$\frac{\partial^2}{\partial t^2} P = N \left[(d_{ee} - d_{gg}) \frac{\partial^2}{\partial t^2} \rho_{ee} + 2 \frac{\partial^2}{\partial t^2} \text{Re}(d_{eg}^* \sigma_{eg} R) \right]. \quad (25)$$

The second term in the bracket reads

$$\begin{aligned}
\frac{\partial^2}{\partial t^2}(d_{eg}^* \sigma_{eg} R) &= d_{eg}^* \left(R \frac{\partial^2}{\partial t^2} \sigma_{eg} + 2 \frac{\partial}{\partial t} \sigma_{eg} \frac{\partial}{\partial t} R + \sigma_{eg} \frac{\partial^2}{\partial t^2} R \right) \\
&= \sum_{n=-\infty}^{\infty} \left[\left(\frac{\partial^2}{\partial t^2} \sigma_{eg} + 2 \frac{\partial}{\partial t} \sigma_{eg} \left(J'_n(\kappa) \frac{\partial}{\partial t} \kappa + i(n-1)\omega J_n(\kappa) \right) \right. \right. \\
&\quad \left. \left. + \sigma_{eg} \left(J''_n(\kappa) \left(\frac{\partial}{\partial t} \kappa \right)^2 + J'_n(\kappa) \frac{\partial^2}{\partial t^2} \kappa + 2i(n-1)\omega J'_n(\kappa) \frac{\partial}{\partial t} \kappa \right. \right. \right. \\
&\quad \left. \left. \left. + [i(n-1)\omega]^2 J_n(\kappa) \right) \right) d_{eg}^* e^{-i(n-1)(kz-\omega t)} \right], \tag{26}
\end{aligned}$$

where we have inserted explicitly the first and second derivatives of R according to Eq. (24). We insert this result back into Eq. (25).

Now, in analogy to the procedure conducted for the left-hand-side (23) of the wave equation, we can separate on the right-hand side terms proportional to different powers of the oscillating factor $\exp[i(kz - \omega t)]$. In the rotating wave approximation, we neglect powers other than 0 and 1, as only these two are present on the left-hand side given by Eq. (23). We now make the important assumption that any cross-talk between the slowly varying terms and those oscillating at the frequency ω can be neglected: The polarization terms oscillating at ω are coupled to the drive while the slowly varying terms act as the source for the signal. This assumption is valid if $\left| \frac{\partial \mathcal{E}_{\text{signal}}}{\partial t} \right| \ll \omega \mathcal{E}_{\text{signal}}$ and similarly for the slowly-varying part of the polarization. In consequence, we can separate two wave equations, describing respectively the dynamics of the drive and of the signal. However, we assume the drive to be strong enough not to be affected by the coupling the medium. The only relevant field equation is therefore the one for the drive, given by (12). On its right-hand side appear the terms corresponding to $n = 1$ in Eq. (26).

C. Numerical approach

The solution of the coupled set of Boch-Maxwell's equations (10,12) can be found numerically.

The wave equation has the form:

$$-\frac{\partial^2}{\partial z^2} f(z, t) + \frac{1}{c^2} \frac{\partial^2}{\partial t^2} f(z, t) = s(z, t), \tag{27}$$

where f is the function we want to find, s is a source term and c is the vacuum speed of the envelope.

Introducing discretization we end up with a time-space grid of evenly distributed points (z_j, t_i) with spatial and temporal steps respectively Δz and Δt . Hence, for space variable we have $z_j = z_0 + j\Delta z$, where $j \in [0, 1, \dots, N_L]$ and N_L is the number of the point at the end of the sample of length L so $N_L \Delta z = L$. Similarly, $t_i = t_0 + i\Delta t$ for $i \in [0, 1, \dots]$ but with no upper bound. For convenience, we denote values of the functions at grid points $f(z_j, t_i) \equiv f_{i,j}$ and $s(z_j, t_i) \equiv s_{i,j}$. By the solution at a time t_{i+1} we understand a set of values $\{f_{i+1,j}\}$ for all j and hence we have to find an expression that depends only on the previously calculated values. This can be done by expressing the second-order derivatives by the three-point (midpoint) formula [32]. Since we solve a second-order partial differential equation, two initial conditions for each space point are required. We introduce values $f_{j,0}$, $s_{j,0}$ and velocities $\partial f_{j,0}/\partial t \equiv g_j$ for the initial time t_0 . In order to reach accuracy of the order of $(\Delta t)^2$, we express $f_{i,j}$ as [33]:

$$\begin{aligned}
f_{i,j} &= \frac{1}{2} \eta^2 (f_{0,j-1} + f_{0,j+1}) + (1 - \eta^2) f_{0,j} + \Delta t g_j + \frac{1}{2} c^2 (\Delta t)^2 s_{0,j}, \\
&\quad \text{for } j \neq 0, N_L, \tag{28}
\end{aligned}$$

and we find

$$f_{i+1,j} = \eta^2(f_{i,j+1} + f_{i,j-1}) + 2(1 - \eta^2)f_{i,j} - f_{i-1,j} + c^2(\Delta t)^2 s_{i,j}, \quad (29)$$

for $i > 0, j \neq 0, N_L$.

Obviously, expressions above are not valid at the ends of the sample. There, we apply transparent boundary conditions [34] for the radiation going out of the sample (for $j = 0, N_L$):

$$\begin{aligned} f_{i,0/N_L} &= \eta^2 f_{0,1/N_L-1} + (1 - \eta^2)f_{0,0/N_L} + (1 - \eta)\Delta t g_{0/N_L}, \\ f_{i+1,0/N_L} &= \frac{2\eta^2 f_{i,1/N_L-1} + 2(1 - \eta^2)f_{i,0/N_L} + (\eta - 1)f_{i-1,0/N_L}}{1 + \eta}, \end{aligned} \quad (30)$$

where we assumed no sources at the ends of the sample. Additionally, we have introduced parameter $\eta = c\Delta t/\Delta z$ so-called Courant number firstly described in [35] whose value is crucial for numerical stability. In our case $\eta = 1$ corresponds to the so-called "magic step" [36] and leads to solution not affected with the numerical dispersion problem.

The source term $s(z, t)$ corresponds to the solution of the Bloch Eqs. (10). The latter is a set of first-order differential equations of one variable for each point in space. At each time step we calculate the solution using the Python build-in method *odeint* from the *scipy.integrate* library. It is a RK4 method so the order of accuracy is $(\Delta t)^4$. This high level of accuracy is required because the source term is eventually differentiated twice, reducing the accuracy to the order of $(\Delta t)^2$. The differentiation is performed using the three-point (midpoint) method.

Our solver is written in Python 2.7, where sets of equations (29, 30) were implemented. A comparison between Eqs. (12) and (27) reveals that $f \equiv E_{\text{signal}}$ and s is the right-hand-side of Eq. (12). The solver is available upon request.

Funding

The authors acknowledge the support from the National Science Centre, Poland grant number 2018/31/D/ST3/01487.

Acknowledgments

The authors thank D. Ziemkiewicz for valuable discussions.

Disclosures

The authors declare no conflicts of interest.

References

1. L. Mandel and E. Wolf, *Optical coherence and quantum optics* (Cambridge university press, 1995).
2. P. Drummond, K. Kheruntsyan, D. J. Heinzen, and R. Wynar, "Stimulated raman adiabatic passage from an atomic to a molecular bose-einstein condensate," *Phys. Rev. A* **65**, 063619 (2002).
3. N. V. Vitanov, A. A. Rangelov, B. W. Shore, and K. Bergmann, "Stimulated raman adiabatic passage in physics, chemistry, and beyond," *Rev. Mod. Phys.* **89**, 015006 (2017).
4. D. Budker, D. Kimball, S. Rochester, V. Yashchuk, and M. Zolotarev, "Sensitive magnetometry based on nonlinear magneto-optical rotation," *Phys. Rev. A* **62**, 043403 (2000).
5. D. Petrosyan and Y. P. Malakyan, "Magneto-optical rotation and cross-phase modulation via coherently driven four-level atoms in a tripod configuration," *Phys. Rev. A* **70**, 023822 (2004).
6. S. Pustelny, D. J. Kimball, S. Rochester, V. Yashchuk, W. Gawlik, and D. Budker, "Pump-probe nonlinear magneto-optical rotation with frequency-modulated light," *Phys. Rev. A* **73**, 023817 (2006).
7. S. E. Harris, "Electromagnetically induced transparency," in *Quantum Electronics and Laser Science Conference*, (Optical Society of America, 1997), p. QTuB1.
8. E. Paspalakis, N. Kylstra, and P. Knight, "Transparency of a short laser pulse via decay interference in a closed v-type system," *Phys. Rev. A* **61**, 045802 (2000).

9. M. Fleischhauer, A. Imamoglu, and J. P. Marangos, "Electromagnetically induced transparency: Optics in coherent media," *Rev. modern physics* **77**, 633 (2005).
10. L. V. Hau, S. E. Harris, Z. Dutton, and C. H. Behroozi, "Light speed reduction to 17 metres per second in an ultracold atomic gas," *Nature* **397**, 594–598 (1999).
11. M. Fleischhauer and M. D. Lukin, "Dark-state polaritons in electromagnetically induced transparency," *Phys. review letters* **84**, 5094 (2000).
12. D. Phillips, A. Fleischhauer, A. Mair, R. Walsworth, and M. D. Lukin, "Storage of light in atomic vapor," *Phys. Rev. Lett.* **86**, 783 (2001).
13. A. Raczynski, K. Slowik, J. Zaremba, and S. Zielińska-Kaniasty, "Controlling statistical properties of stored light," *Opt. communications* **279**, 324–329 (2007).
14. K. Slowik, A. Raczynski, J. Zaremba, and S. Zielińska-Kaniasty, "Light storage in a tripod medium as a basis for logical operations," *Opt. Commun.* **285**, 2392–2396 (2012).
15. O. Kibis, G. Y. Slepyan, S. Maksimenko, and A. Hoffmann, "Matter coupling to strong electromagnetic fields in two-level quantum systems with broken inversion symmetry," *Phys. review letters* **102**, 023601 (2009).
16. I. Savenko, O. Kibis, and I. A. Shelykh, "Asymmetric quantum dot in a microcavity as a nonlinear optical element," *Phys. Rev. A* **85**, 053818 (2012).
17. G. Y. Kryuchkyan, V. Shahnazaryan, O. V. Kibis, and I. Shelykh, "Resonance fluorescence from an asymmetric quantum dot dressed by a bichromatic electromagnetic field," *Phys. Rev. A* **95**, 013834 (2017).
18. E. Paspalakis, J. Boviatsis, and S. Baskoutas, "Effects of probe field intensity in nonlinear optical processes in asymmetric semiconductor quantum dots," *J. Appl. Phys.* **114**, 153107 (2013).
19. M. Marthaler, M. Koppenhöfer, K. Slowik, and C. Rockstuhl, "Lasing at arbitrary frequencies with atoms with broken inversion symmetry and an engineered electromagnetic environment," *arXiv preprint arXiv:1601.01511* (2016).
20. M. Koppenhöfer and M. Marthaler, "Creation of a squeezed photon distribution using artificial atoms with broken inversion symmetry," *Phys. Rev. A* **93**, 023831 (2016).
21. I. Y. Chestnov, V. A. Shahnazaryan, A. P. Alodjants, and I. A. Shelykh, "Terahertz lasing in ensemble of asymmetric quantum dots," *Acs Photonics* **4**, 2726–2737 (2017).
22. M. Tamanis, M. Auzinsh, I. Klincare, O. Nikolayeva, R. Ferber, E. Pazyuk, A. Stolyarov, and A. Zaitsevskii, "Nak λ doubling and permanent electric dipoles in low-lying 1π states: Experiment and theory," *Phys. Rev. A* **58**, 1932 (1998).
23. M. Aymar and O. Dulieu, "Calculations of transition and permanent dipole moments of heteronuclear alkali dimers nak, narb and nacs," *Mol. Phys.* **105**, 1733–1742 (2007).
24. G. Lindblad, "On the generators of quantum dynamical semigroups," *Commun. Math. Phys.* **48**, 119–130 (1976).
25. V. Gorini, A. Kossakowski, and E. C. G. Sudarshan, "Completely positive dynamical semigroups of n-level systems," *J. Math. Phys.* **17**, 821–825 (1976).
26. M. Scully and M. Zubairy, *Quantum Optics* (Cambridge University Press, 1997).
27. D. Dziczek and S. Chwirot, "Dual control of slow light in reciprocal electromagnetically-induced-transparency conditions," *Phys. Rev. A* **79**, 043807 (2009).
28. K. Inomata, Z. Lin, K. Koshino, W. D. Oliver, J.-S. Tsai, T. Yamamoto, and Y. Nakamura, "Single microwave-photon detector using an artificial λ -type three-level system," *Nat. communications* **7**, 1–7 (2016).
29. J.-C. Besse, S. Gasparinetti, M. C. Collodo, T. Walter, P. Kurpiers, M. Pechal, C. Eichler, and A. Wallraff, "Single-shot quantum nondemolition detection of individual itinerant microwave photons," *Phys. Rev. X* **8**, 021003 (2018).
30. C. M. Bowden and J. P. Dowling, "Near-dipole-dipole effects in dense media: Generalized maxwell-bloch equations," *Phys. Rev. A* **47**, 1247 (1993).
31. R. Loudon, *The Quantum Theory of Light* (OUP Oxford, 2000).
32. R. L. Burden and J. D. Faires, *Numerical Analysis* (Brooks/Cole, Cengage Learning, 2011).
33. P. J. Oliver, "Numerical analysis lecture notes," (2008).
34. D.-C. Ionescu and H. Igel, "Transparent boundary conditions for wave propagation on unbounded domains," in *International Conference on Computational Science*, (Springer, 2003), pp. 807–816.
35. R. Courant, K. Friedrichs, and H. Lewy, "On the partial difference equations of mathematical physics," *IBM journal Res. Dev.* **11**, 215–234 (1967).
36. M. Min and C. Teng, "The instability of the yee scheme for the Δt magic time step Δt ," *J. Comput. Phys.* **166**, 418–424 (2001).